Eur. Phys. J. B **37**, 177–185 (2004)
DOI: 10.1140/epjb/e2004-00044-x

THE EUROPEAN PHYSICAL JOURNAL B

Magnetization and configurational anisotropy in magnetic clusters: Monte Carlo simulation

Zhigao Huang[1,2,a], Zhigao Chen[1,2], Fengming Zhang[1], and Youwei Du[1]

[1] National Laboratory of Solid State Microstructures, Nanjing University, Nanjing 210093, P.R. China
[2] Department of Physics, Fujian Normal University, Fuzhou, 350007, P.R. China

Received 31 May 2003 / Received in final form 10 September 2003
Published online 15 March 2004 –

Abstract. Based on the Monte Carlo simulation, the magnetic properties of the clusters, e.g. magnetization, Curie temperature, hysteresis, coercivity, natural angle and energy distribution etc., have been calculated. It has been found that, for the pure ferromagnetic cluster, the $T^{3/2}$ Bloch law is well satisfied at low temperature ($T < 0.5T_C$) and B_{sur} is equal to $3B_{bulk}$. Meanwhile, there are clear indications that B increases drastically with the reducing atomic number N which is consistent with the experimental facts. The results have been evaluated using the Bloch exponent law in the approximate crystalline approximation. It has also been demonstrated that the size dependence of the Curie temperature can be described by finite-size scaling theory. The investigation of the hysteresis and the spin configurations in different magnetization processes reveals the existence of an easy magnetization direction and anisotropy. The thermal coercivity for the clusters with zero and finite uniaxial anisotropy matches the experimental results well. The simulated results for the natural angle and energy distribution in the clusters prove further the existence of the configurational anisotropy in the clusters. It has been discussed that the natural angle and energy distribution influence the hysteresis of a cluster.

PACS. 75.75.+a Magnetic properties of nanostructures – 75.40.Mg Numerical simulation studies – 75.60.Ej Magnetization curves, hysteresis, Barkhausen and related effects – 75.40.Cx Static properties (order parameter, static susceptibility, heat capacities, critical exponents, etc.)

1 Introduction

Nanostructured magnets have become a rich and rapidly growing new area in condensed matter physics due to their many potential applications in high density memory devices and magnetic field sensing, such as MRAM (magnetic random access memory) and spin-valve magnetic field sensors. Magnetic clusters are not only used as the magnetic nanoelements in microelectronic devices, but also provide a link between the magnetism of the materials at the microscopic atomic level and the macroscopic level. Recently, magnetic clusters in molecular beams, metals and semiconductors have become hot topics in the area of magnetism and magnetic materials [1]. The free clusters were obtained from molecular beams [2–4]. It is important for understanding the magnetism of a cluster to probe the properties of an individual one instead of an ensemble by ignoring the interaction between both clusters or between a cluster and the surrounding medium. A large magnetoresistance (*MR*) has been observed in magnetic granular films [5] and tunnel-type nanostructures, such as $Co/Al_2O_3/CoFe$ tunnel junctions [6], polycrystalline $Zn_{0.41}Fe_{2.59}O_4$ [7], half-metallic Fe_3O_4 [8] etc. It is thought that such a large *MR* results from the intrinsic properties of clusters and the relative orientation of magnetic moments between clusters [9–12]. Diluted magnetic semiconductors have been proposed as possible materials for spintronic devices. Recently, n-type $Zn_{1-x}M_xO$ (M = Co, Ni, Cr and Mn) magnetic semiconductors have attracted attention because of their high ferromagnetic Curie temperature [13–15]. However, it is indicated that the origin of the ferromagnetism in $Zn_{1-x}Co_xO$ is attributed to the Co cluster [13].

Many interesting phenomena have been demonstrated in nanoparticles such as superparamagnetism and slow exponential relaxation rates at low temperature. However, for clusters with a radius of several nanometers, the picture of a single-domain magnetic particle, in which all spins point in the same direction and coherent relaxation processes are produced, is not valid as surface effects become really crucial. In fact, the magnetic properties of the cluster are strongly affected by its finite-size and surface. The effects increase with the decrease of the cluster size. Surface effects originate from the symmetry-breakdown

[a] e-mail: zghuang@fjnu.edu.cn

of the crystal structure at the boundary of the cluster, while the finite-size effects are due to the nanoscale size of the materials. To explain the observed reduction of the saturation magnetization in magnetic nanoparticles, a model of random canting of the spins at the particles' surface caused by competing antiferromagnetic exchange interactions at the surface was suggested at first by Coey [16]. Since then, the arguments as to the origin of the reduction of the saturation magnetization in magnetic nanoparticles have begun. Recently, some experimental results support a surface-spin-disorder origin for the reduction [17–19]; while other results indicate a finite-size-effect origin [20,21]. Therefore, no conclusive explanation for the issue has been reached yet. In addition, up to now, the inconsistency of the Bloch constant and Bloch exponent obtained from different theoretical and experimental work still exists [22–27].

Of fundamental importance are the hysteresis and anisotropy for ferromagnetic materials. The anisotropy refers to the presence of preferred magnetization directions and may arise from the symmetry of the electronic Fermi surface, the strain and the shape of the materials. Specially, for a nanomagnet, the shape has a very important influence on its anisotropy. Recently, a new interesting concept called configurational anisotropy was suggested by Cowburn [28]. It comes from the differences in the energy of the different configurations caused as the magnetization direction is varied. The configurational anisotropy in elliptical, triangular, square, pentagonal and circular geometries has been considered [28–31]. However, up to now the configurational anisotropy of the cluster has scarcely been observed.

In order to explain the exchange bias, another important concept called 'natural' angle was proposed by Stamps et al. [32,33]. This angle is named as the equilibrium orientation of the ferromagnet in zero applied field. The classical mechanism of hysteresis and coercivity caused in the processes of boundary movement and the single domain rotation was well described in 1947 by Stoner and Wohlfarth [34]. For an individual nanomagnet with its size and surface effects, however, Stoner and Wohlfarth's theory is not valid. Hence it could be interesting to study the correlations among the hysteresis, anisotropy, natural angle and spin configuration in nanomagnet.

This paper is organized as follows. In Section 2, we outline a simulation model based on the Heisenberg interaction and the Monte Carlo method. In Section 3.1, the results on the thermal magnetization and Curie temperature of the cluster are presented. In Section 3.2, the hysteresis and the thermal coercivity for the clusters with zero and finite uniaxial anisotropy are studied. An easy magnetization direction and an anisotropy resulted from the spin configurations of the pure ferromagnetic clusters are found. In Section 4, the natural angle and energy distribution with a probing applied field are calculated. A systematic theoretical analysis for establishing the relationship between natural angle and coercivity is presented. In Section 5, a conclusion is given.

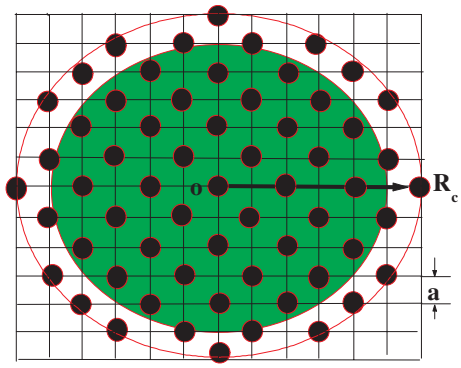

Fig. 1. A schematic cross-section of the atomic arrangement in the spherical cluster.

2 Model and simulation technique

The total spin Hamiltonian of a cluster is described by the following:

$$H_s = -\sum_{\langle ij \rangle} J_{ij} \vec{S}_i \cdot \vec{S_j} - K \sum_i (S_i^z)^2 - H \sum_i S_i^z \qquad (1)$$

where $\sum_{\langle ij \rangle}$ is performed over the spin pairs at nearest-neighbor (NN) sites i and j with an exchange interaction J_{ij}, K is the uniaxial anisotropy with easy axis along the z axis. For the case with $K = 0$, the cluster is named as the pure ferromagnetic (PFM) cluster. It is calculated with $\left|\vec{S}_i\right| = 1$. It is assumed that the cluster is a spherical shaped particle with radius R_c and FCC structure, and the radius of the core is R_{core}. A schematic cross-section of the atomic arrangement in the spherical cluster is shown in Figure 1. It is assumed that the thickness of the surface shell in the boundary area, $R_c - R_{core}$, is a constant, a, and only the variation of particle size is allowed. In the simulation, a is set as half of the lattice constant and is taken as the reduced unit ($a = 1$). It can be calculated that the values of 10, 9, 8, 7, 6, 5, 3.75, 3 for R_c correspond to the total numbers of atoms of 2123, 1505, 1061, 683, 459, 249, 135, 55, in the cluster, respectively. As an example, we consider a FCC spherical cluster containing 2123 magnetic atoms ($N = 2123$) and 48 shells corresponding $R_c = 10$. It is found that the outermost incompletely filled shells of the cluster have a complex coordination structure, with different coordinate numbers for the atoms in different shells [35]. The 39th shell corresponding $R_{core} = 9$ is defined as a boundary, and then the area from 39th to 48th shell is named as the surface, while the one from the first to 39th is defined as the core. The exchange interaction J_{ij} in equation (1) between sites i and j is taken as J. Here, J is used as unit of temperature and energy, and we let $J = 1$. Free boundary conditions are applied in all directions. To minimize the finite size effects and compare them with the results of the clusters, we have used at the same time periodic boundary (PB) conditions for a system of large enough size ($L \times L \times L$ block) with a FCC structure and the zero uniaxial anisotropy. In our simulation L is taken as 20.

Next, let us simulate spin configurations of the block and magnetic clusters using the standard Monte Carlo-Metropolis (MC) [36]. The method of this algorithm can be found in our previous work [11,35]. To reproduce the experimental measurements of the zero field-cooled system and the field-cooled one, we started from a random configuration in the high temperature region and followed the quasicontinuously cooling process down to the measured temperatures of the system with or without the magnetic field at a constant temperature step $T = -0.05 - 0.1$. 400 Monte Carlo steps (MCS) were performed at each temperature. The hysteresis loops were computed by starting from a demagnetized state at $H = 0$ and increasing quasicontinuously the magnetic field to H_m, then decreasing to $-H_m$ before increasing to $+H_m$. In the processes, ΔH was taken as 0.05 and the magnetization was averaged over 2000 MCS at each field. In order to measure the natural angle and the spatial distribution of energy under different external magnetic field directions, the spherical polar coordinates θ and φ were divided into $N_n (= N_1 \times N_2)$ orientations (θ_l, φ_m), where $\theta_l = 0, \pi/N_1, 2\pi/N_1, 3\pi/N_1, ..., l\pi/N_1, ..., \pi$; $\varphi_m = 0, \pi/N_2, 2\pi/N_2, 3\pi/N_2, ..., 2\pi$. In the simulation, we set $N_1 = 18$ and $N_2 = 36$. The direction of each spin in the magnetic cluster always locates in an orientation angle (θ_l, φ_m). Therefore updating the spin orientation by visiting each atomic site, we can obtain the spatial distribution of the spin orientation. If the equilibrium spin configuration in the magnetic cluster in a zero applied field is obtained, the number of spins N_l orientating along θ_l can be obtained, and the average natural angle can be computed by $\overline{\theta} = \sum_l \theta_l N_l / \sum_l N_l$. To obtain the equilibrium spin configuration, the first 10^4 MCS per spin were discarded and the average was taken over with the next 3000 MCS. As the configurational anisotropy arises from the energy difference between the different configurations of the nanomagnet when one magnetizes the nanomagnet along different directions [28,30], here we let the applied field be along different orientations (θ_l, φ_m) and calculate their corresponding energies. Thus we can get the spatial energy distribution. This is equivalent to the calculation of the energy of the nanomagnet in a fixed applied magnetic field when one rotates it around a center point. For every direction of the applied field, the first 5000 MCS per spin were discarded and the average for the equilibrium was taken over the next 3000 MCS. In addition, the specific heat was calculated by $C = (\langle E^2 \rangle - \langle E \rangle^2)/(N_e T^2)$. Here, E is the energy of the system and N_e is the number of spins of the system.

3 Simulated results and discussion

3.1 Thermal magnetization and curie temperature

At first, the size and surface effects of the magnetization for the PFM clusters were considered. Figure 2 shows the magnetization of the core, the surface and the whole cluster as a function of the temperature with $N = 2123$. It is found that the magnetization curve at the surface is different from the one for the core, and the reduction ratio of the magnetization with increasing temperature for the surface is larger than the one for the core, which is consistent with the surface magnetic properties of γ-Fe_2O_3 particles obtained by Horio et al. [37] which reveals clearly the surface effect. Figure 3 shows the typical M vs. T curves of the clusters with $N = 55$, 249, 2123 and the block with the PB condition, respectively. It is found that at low temperature, the $T^{3/2}$ Bloch law with the Bloch constant B, $M(T) = M(0)(1 - BT^{3/2})$ [17,35], is obeyed well for clusters with atomic numbers from 55 to 2123 and for the block. Here, T is the reduced temperature corresponding to the one used in the simulation. It is evident that below the Curie temperature magnetization increases with the size of cluster, which is similar to results reported by Merikoshi et al. [38]. For $N = 2123$, it was found that $B_{sur} = 0.0468$, $B_{core} = 0.0245$, $B_{PB} = 0.0248$, $B_{bulk} = 0.0147$. Obviously, $B_{sur} = 2B_{core} = 2B_{PB}$,

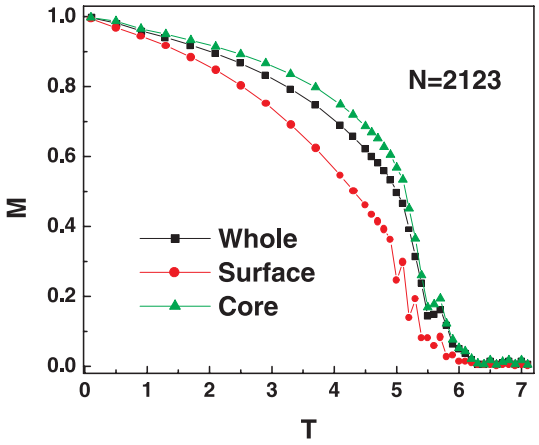

Fig. 2. The magnetization of the core, the surface and the whole PFM cluster as a function of temperature with $N = 2123$.

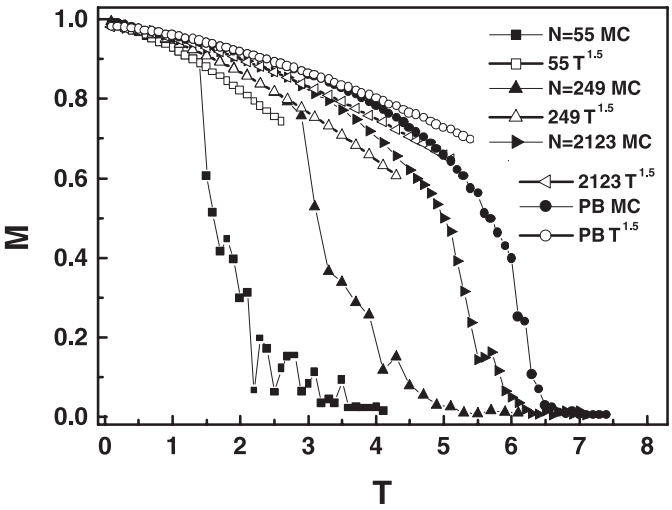

Fig. 3. Magnetization as a function of temperature for the PFM clusters with $N = 55$, 249, 2123 and the block with the PB condition.

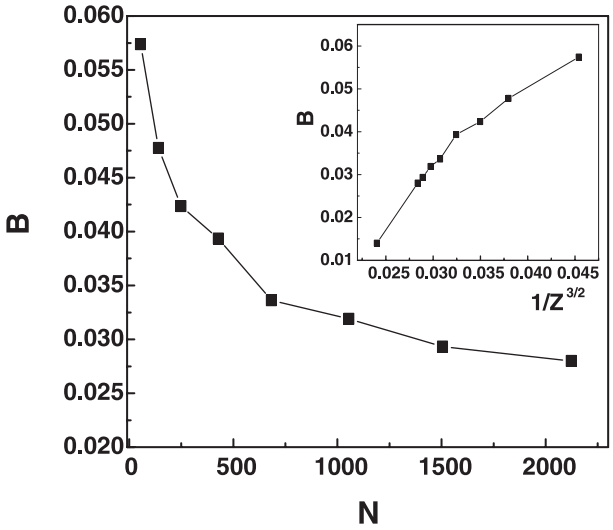

Fig. 4. The N dependence of B for the PFM cluster; the inset represents B as a function of $Z^{-3/2}$.

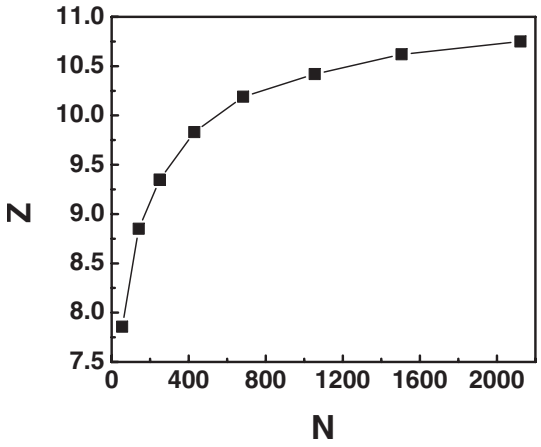

Fig. 5. The average coordination number Z as a function of N for the FCC spherical PFM cluster.

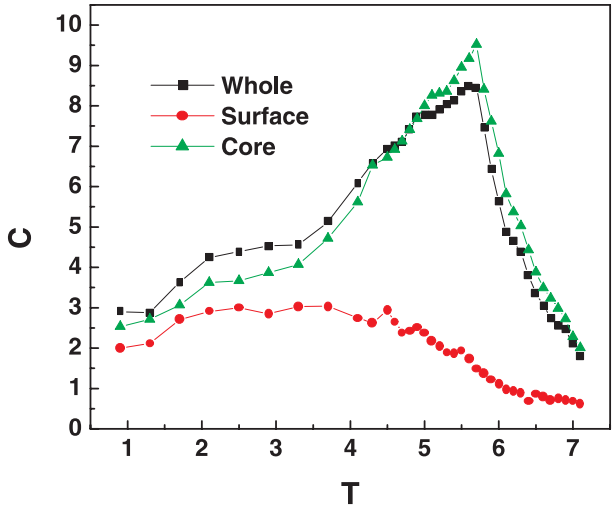

Fig. 6. The simulated temperature dependence of the specific heat in the surface, the core and the whole PFM cluster with $N = 2123$.

$B_{sur} = 3B_{bulk}$, which is in accordance with the experimental results obtained by Pierce et al. for the magnetization of a macroscopic surface [22,24] and the prediction of Mills et al. [39–41] The N dependence of B is shown in Figure 4, and the inset represents B as a function of $Z^{-3/2}$. Here Z is the coordination number. From the figure, two important results are obtained: firstly, B increases drastically with reducing N, consistent with the experimental results on crystalline iron reported by Zhang [23,27]; secondly, B is approximately proportional to $Z^{-3/2}$ in both the different slopes, which can be explained by spin wave excitation theory in the approximate crystalline approximation. Ferromagnetic magnons have a quadratic dispersion relation at small wave vector q, $\hbar\omega(q) = Dq^2$, where D is the spin wave stiffness constant. The spin wave stiffness constant is, in the approximate crystalline approximation, expressed by the following [42]

$$D = D(0)[1 - 2Z(\Delta b/b)\delta] \tag{2}$$

where $D(0) = ZSJb^2/3$, with b as the distance between the nearest-neighbor (NN) atoms, J is the exchange constant, S is atom spin, ν_0 is the atom volume, $\langle b\rangle^2$ is the the mean-square deviation of NN pair distance and δ is the the structure fluctuation or exchange interaction fluctuation. Based on the relation between the Bloch coefficient and the spin wave stiffness constant [17,42–44], and equation (2), we can derive the Bloch law, $M(T) = M(0)(1 - BT^{3/2})$, where the Bloch coefficient B can be expressed by

$$B = 2.612\nu_0 \left(3/4\pi Sb^2\right)^{3/2} [Z(1 - 2Z(\Delta b/b)\delta]^{-3/2} \propto [Z]^{-3/2} [1 - 2Z(\Delta a/a)\delta]^{-3/2}. \tag{3}$$

The first term of equation (3) represents the influence of the coordination number on B, the second one reflects the role of the structure and exchange fluctuations on B. It can be seen from Figure 5 and equation (3) that the dependence of B on both N and $Z^{-3/2}$ is in agreement with that indicated in Figure 4. The change of slope in the inset of Figure 4 can be explained by the structure and exchange interaction fluctuation $(\Delta b/b)\delta$ increasing with decreasing Z. It is assumed that $(\Delta b/b)\delta \propto 1/(c+Z)$, where c is a constant. Then, we can obtain that the slope of B to $Z^{-3/2}$ decreases with decreasing Z, which explains well the results in Figure 4.

Figure 6 shows the simulated temperature dependence of the specific heat of the surface, the core and the whole PFM cluster with $N = 2123$. While, the specific heat as a function of the temperature for the PB block and the ones for different whole PFM clusters with $N = 135$, 249 and 2123 are plotted in Figure 7. It can be noted that there exist sharp peaks for the PB block and the cluster with a large number of the atoms (such as $N = 2123$). However, broad peaks of the specific heat are found for the surface of the cluster with $N = 2123$ and for whole clusters with a small number of atoms (such as $N = 249$ and 135), which is an obvious illustration of the

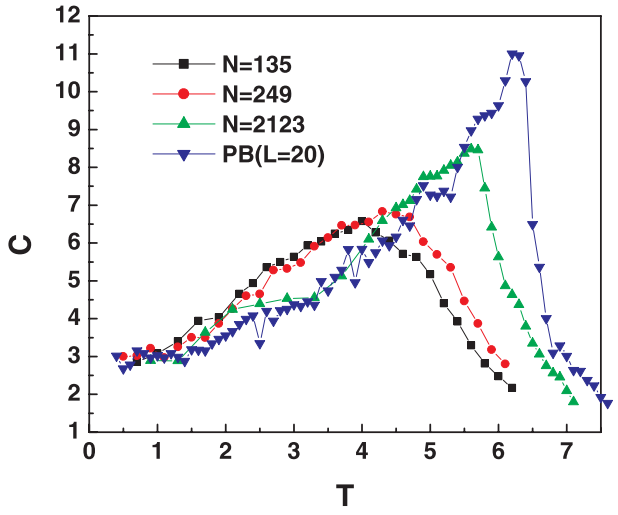

Fig. 7. The specific heat as a function of the temperature for the PB block (8×10^3) and the different PFM clusters with $N = 135$, 249 and 2123.

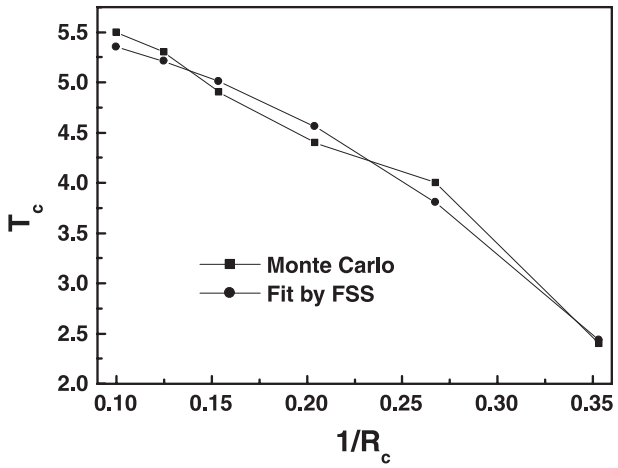

Fig. 8. The size dependence of the transition temperature T_c for the PFM clusters.

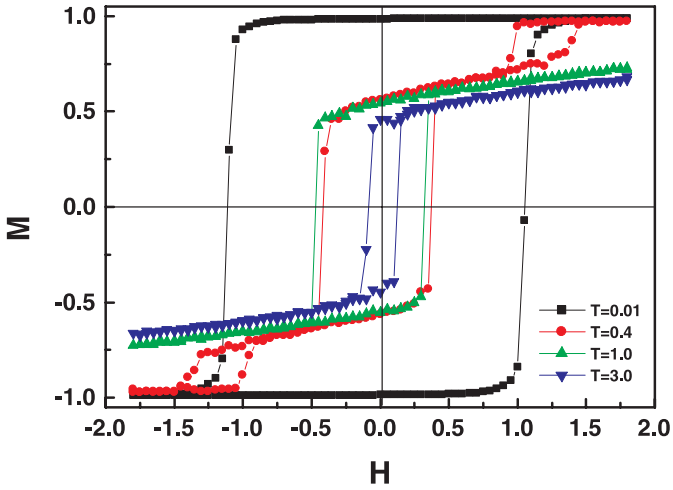

Fig. 9. The hysteresis loops of the PFM cluster with the number of the atoms $N = 249$ at $T = 0.01$, 0.4, 1.0 and 3.0, respectively.

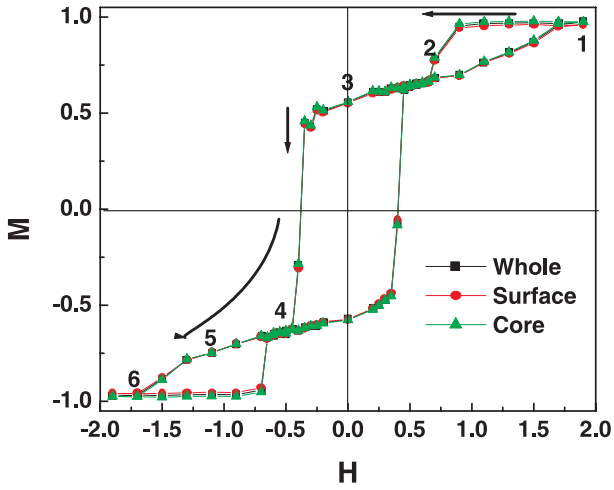

Fig. 10. The hysteresis loops in the surface, the core and the whole PFM cluster with $N = 249$ at $T = 0.4$.

finite-size and surface effects. The simulated results are similar to the experimental results for the maghemite γ-Fe_2O_3 nanoparticles [45]. The sharp peaks in the figures clearly indicate a second order transition from a paramagnetic to ferromagnetic phase. The cluster size dependence of the transition temperature, T_c, can be obtained and is plotted in Figure 8. It is found that finite-size scaling (FSS) [46,47] can be used to explain the behavior of T_c. In this theory it is predicted that the shift in the transition temperature T_c from that of the bulk should depend on the dimension of the system as described by

$$[T_c(\infty) - T_c(R_c)]/T_c(\infty) = (R_{c0}/R_c)^{1/\upsilon} \qquad (4)$$

where $T_c\,(R_c)$ is the Curie temperature of the cluster with radius R_c, $T_c\,(\infty)$ is that of the bulk, υ and R_{c0} are the critical exponent and microscopic scale length with expected values of 1.86 ± 0.03 and 0.49 ± 0.03, respectively. The fitted size dependence of the Curie temperature with equation (4) is also shown in Figure 8. The fitted parameters are $R_{c0} = 1.86 \pm 0.08$, $\upsilon = 0.50 \pm 0.07$. It is demonstrates convincingly that the simulated results are consistent with the ones from the scaling law [46,47] and the experiments [27].

3.2 Hysteresis loop and coercivity

Figure 9 shows the hysteresis loops of the PFM cluster with the number of atoms $N = 249$ at different temperatures. The typical hysteresis loops in the surface, the core and the whole PFM cluster with $N = 249$ at $T = 0.4$ are shown in Figure 10. The cross sections of the spin configurations at different magnetization levels corresponding to the loops in Figure 10 are shown schematically in Figure 11. The hysteresis loops of the PFM clusters, and the FM clusters with uniaxial anisotropy $K = 1.0$ for $N = 2123$, 249, 55 at $T = 1.0$ are presented in Figure 12. From Figures 9–12, it is found that the loops of the clusters at very low temperature are perfectly square. In the

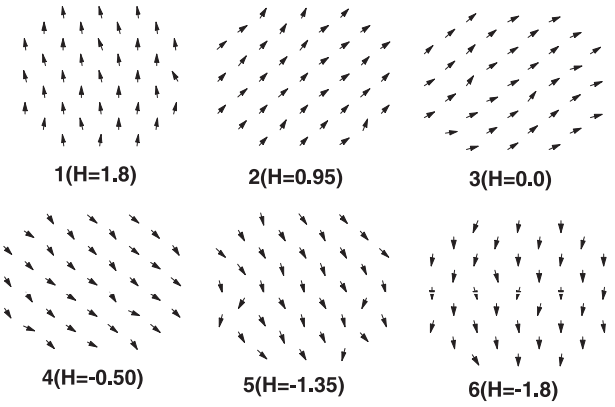

Fig. 11. The spin configurations at different magnetization levels corresponding to the loops in Figure 10.

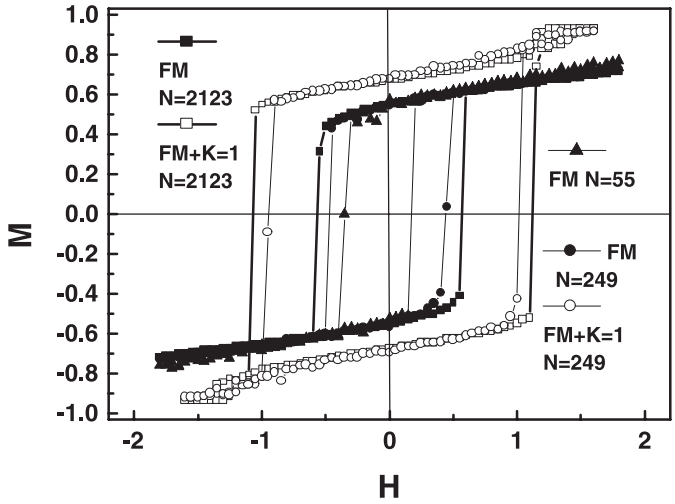

Fig. 12. The hysteresis loops of the PFM clusters, and the FM cluster with uniaxial anisotropy $K = 1.0$ for $N = 2123$, 249, 55 at $T = 1.0$.

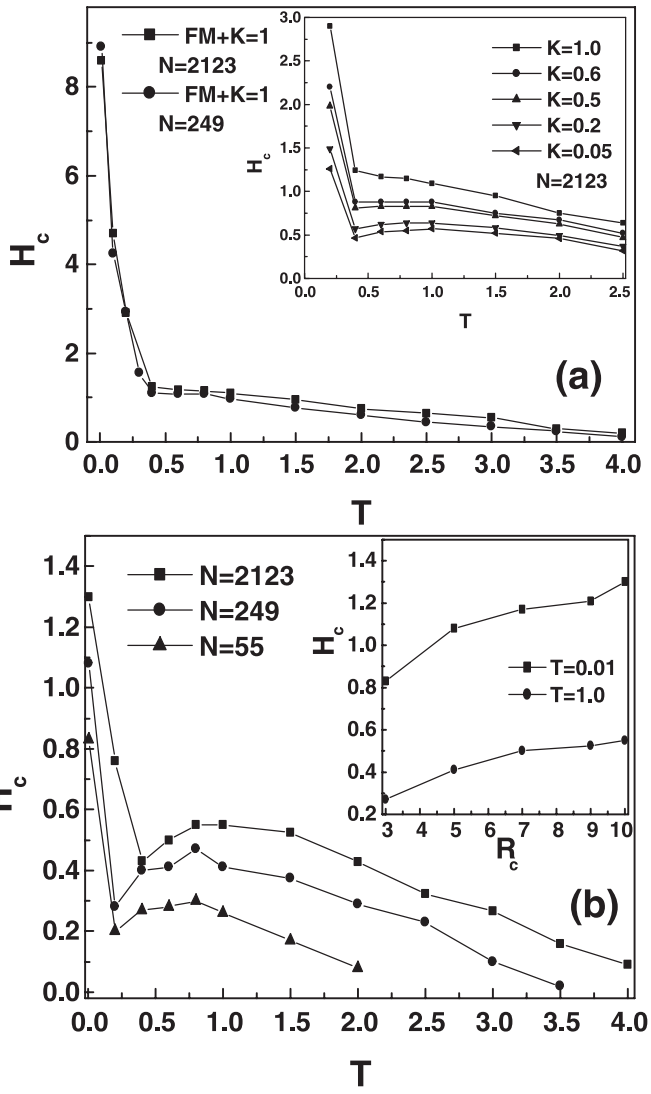

Fig. 13. (a) The coercivity as a function of temperature for the FM clusters with $K = 1$ for $N = 2123$ and 249, respectively. The inset in the figure presents the coercivity as a function of temperature for FM clusters with N=2123, $K = 0.6, 0.5, 0.2$ and 0.05, respectively. (b) the temperature dependence of the coercivity for the PFM clusters with $N = 2123$, 249 and 55, respectively. The inset in the figure represents the coercivity as a function of the radius of the PFM cluster at $T = 0.01$ and 1.

medium range of temperature such as $T = 0.2 - 0.8$, three jumps are found in the loop curves seen in Figure 10. At higher temperature, the loops of the clusters reveal a progressive magnetization with a single jump, and both the saturation field and the high field susceptibility increase as the cluster size decreases or the temperature increases, which represents a typical feature associated with spin disorder due to the finite-size and surface effects. From Figures 10 and 11, one can find two interesting phenomena. Firstly, there is almost no difference between the loops of the surface and the core except that the magnitude of the magnetization in the surface is slightly smaller than the one in the core, indicating that coherent and collective behaviors exist in the PFM cluster. This is different from the results for a cluster with surface anisotropy and maghemite nanoparticles [48,49]. Secondly, a clear easy axis is found to exist in the PFM clusters, which will be discussed in detail in the next section.

Shown in Figure 13a is the coercivity as a function of temperature for the FM clusters with $K = 1$ and $N = 2123$ and 249, respectively. The inset in the figure shows the coercivity as a function of temperature for FM clusters with $N = 2123$, $K = 0.6, 0.5, 0.2$ and 0.05, respectively. Figure 13b represents the coercivity as a function of temperature for the PFM clusters with $N = 2123$, 249 and 55, respectively, and the coercivity as a function of the radius of the PFM cluster at $T = 0.01$ and 1 is presented in the inset of the figure. According to the work of Bean and Pfeiffer et al. [50,51], the temperature dependence of the coercivities for the particles can be expressed as

$$H_c(T) = H_c(0)[1 - c_\alpha T^\alpha] \tag{5}$$

where $H_c(0)$ is the coercivity at $T = 0$ K, c_α is a parameter related to the anisotropy, the volume of the

particle and the measuring time. The exponent has a magnitude of $\alpha = 0.5$ for an assembly of aligned particles [50] and $\alpha = 0.77$ for randomly oriented particles [51]. The simulated temperature dependence of the coercivity in Figure 13 reveals that the coercivity decreases dramatically with increasing temperature in the low temperature region ($T < 0.40$), remains basically constant at the medium temperature region, and drops again with increasing temperature in the high temperature region. Therefore, the temperature dependence of the coercivity does not fit the T^{α} law over the whole temperature region. In contrast, however, it can be described by the T^{α} law in the low and high temperature regions. The simulated results are consistent with the experimental facts for ultra-fine iron particles [52], nanometer sized iron clusters [53], γ-Fe_2O_3 nanoparticles [18,54] and $Co_{0.2}Zn_{0.8}$-Fe_2O_4 spinel oxide [55]. As presented in Figure 13, the behaviour of the temperature dependence of the coercivity relies on the value of K. For $K > 0.6$, the coercivity changes monotonously with the temperature; while there exists a dip in the curve when $K < 0.6$. Comparing Figure 13a with 13b, one finds that although the magnitudes of coercivity for the clusters with uniaxial anisotropy are much larger than those for the PFM clusters, the thermal change trends of coercivities for them are similar, which means that a new uniaxial-like anisotropy should exist in the PFM clusters. These phenomena will be discussed in the next section. One can note also from Figure 13b that the coercivity increases with increasing size of the cluster.

3.3 Natural angle and configurational anisotropy in magnetic cluster

The natural angle is defined as the equilibrium orientation of the ferromagnet in a zero applied field, which means, in fact, an easy magnetization direction. It can be determined by averaging the orientation of the spins in the zero applied field or the spatial distribution of the energy with a probing applied field. Figure 14 shows the typical spatial distribution of the orientations of the spins for the PFM cluster in the zero applied field with $N = 249$ at $T = 0.40$. From Figure 14, it is found that the orientations of the spins are concentrated within $\theta = 0.5 - 1.4$ and $\phi = 3.5 - 4.5$, and the average orientation (it is also called the nature angle) $\overline{\theta}$ is equal to 0.88, which is presented in Figure 15. The number of spatial orientations, (θ_l, φ_m) with $l = 1, 2, ..., 18$ and $m = 1, 2, ..., 36$, for the spins was set as N_n ($N_1 \times N_2$), and the energies of the cluster were calculated as the external field $H = 0.5$ is applied along the orientations, respectively. So, we can obtain the spatial distribution of the energy. As for every θ_l, there are N_2 energies corresponding to N_2 different angles φ_m. In order to simplify the question, a minimum energy E_l corresponding to θ_l orientation is found from the N_2 energies. Shown in Figure 15 is the minimum energy E_l as a function of θ_l for the PFM cluster with $N = 249$ at $T = 0.40$. From the figure, it can be seen that the orientation for the minimum energy obtained from the calculated spatial distribution of the energy of the cluster is consistent with

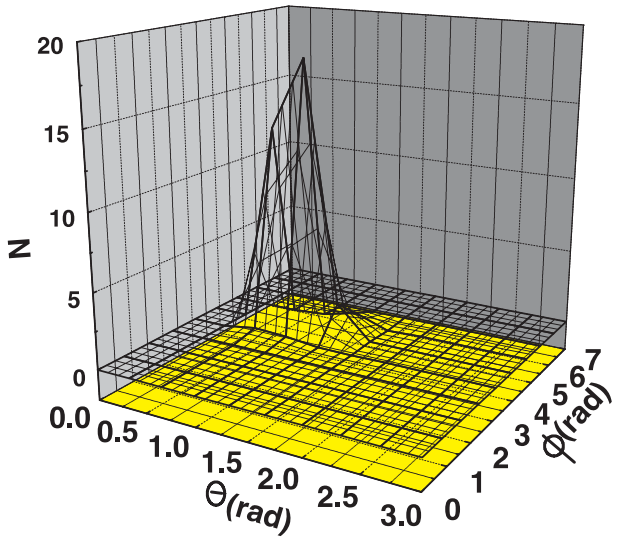

Fig. 14. The typical spatial distribution of the orientation of the spins for the PFM cluster with $N = 249$ at $T = 0.40$.

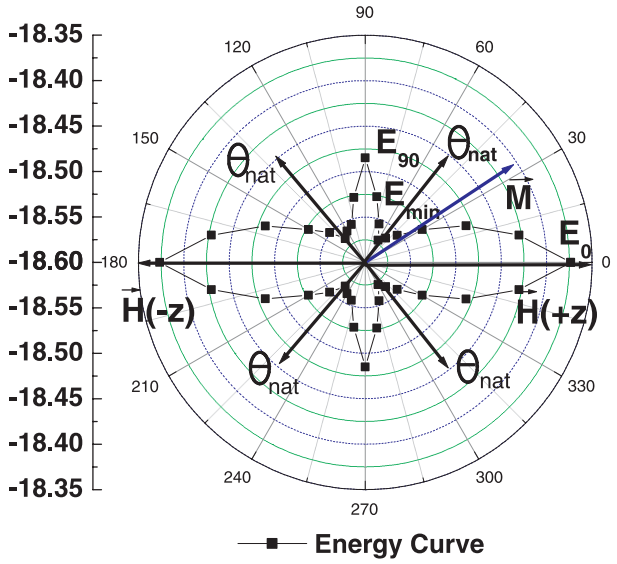

Fig. 15. The minimum energy E_l as function of θ_l by the probing the applied field $H = 0.5$ for the PFM cluster with $N = 249$ at $T = 0.40$. θ_{nat} corresponds to the average angle in Figure 14.

the natural angle as shown in Figure 14. Figure 16 shows the temperature dependence of the natural angle for the PFM clusters with $N = 2123$, 249 and 55, respectively. From the figure, it is found that the natural angle is near zero at very low temperature, which is consistent with the square loop at $T = 0.01$ as seen in Figure 9. As shown in the figure, with a very small increase of temperature just above the zero point, the natural angle rises sharply to about 0.88 radians (50°), then it remains almost stable at $\theta_{nat} = 50°$ up to the temperature region near the Curie

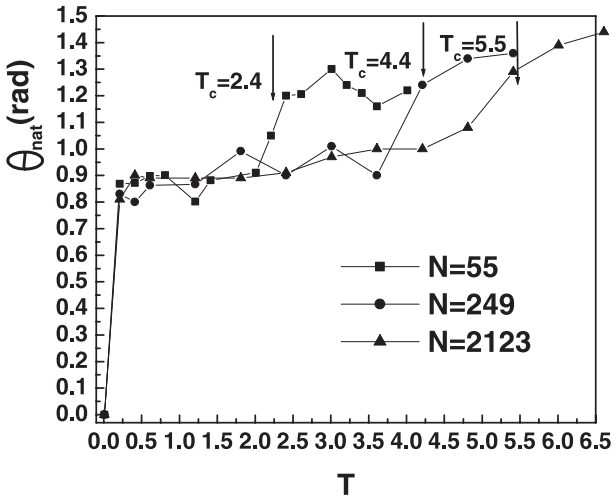

Fig. 16. The temperature dependence of the natural angle for the PFM clusters with $N = 2123$, 249 and 55, respectively.

temperature for all the clusters. However, for $T > T_c$, the natural angle increases dramatically and is close to 1.507 radians (90°) for the clusters, which results from the disorder of the spins. The natural angle and energy distribution as seen in Figures 14–16 indicate clearly the existence of the configurational anisotropy for the PFM clusters of zero anisotropy at $K = 0$.

Now from the natural angle and configurational anisotropy let us discuss the magnetization behaviors of the clusters as seen in Figures 9–13. As the thermal energy k_BT is zero at $T = 0$ K, the magnitude of the magnetization does not change obviously until the reversal point where the magnetization jumps to its new metastable state. The jump occurs when the Zeeman energy is above the barrier for the anisotropy energy. Thus, the loop has a square shape at very low temperature ($T < 0.2$). In the medium range of temperature ($0.2 < T < 0.8$), the loop shape and the spin configurations of the cluster in the magnetization processes as found in Figures 10 and 11 can be interpreted as the result of a competition between the different energies, including the configurational anisotropy energy E_K, Zeeman energy E_h and thermal energy K_BT. As the applied field is large enough to overcome the thermal fluctuation, the spins are forced along the direction of the applied field (Z axis) and remain at about 1. As the applied field decreases, the Zeeman energy is below the thermal energy, which causes the re-orientation of spins to the easy magnetization direction as seen in the states '2', '3' in Figures 10–11. With the increase of a reverse applied field, the Zeeman energy, which has already become positive as $H < 0$, and thermal energy together reverse the spins by overcoming the barrier. When the magnitude of the applied field increases to the value of the coercivity, the spins jump to another easy magnetization direction as shown in state '4'. As the applied field increases further along negative Z-axis direction, the spins are forced to rotate to the negative direction of the z-axis. At higher temperature ($T > 0.8$), the thermal energy is larger than the Zeeman energy, which allows the spins to be initially in the easy magnetization direction. Therefore only one coherent-jump exists as seen in Figures 9 and 12.

It has been reported that the barrier height of the cluster resulting from the configurational anisotropy decreases slightly with decreasing temperature due to the decrease of the disorder freedom of the spins, which gives rise to the decrease of the coercivity with decreasing temperature [56]. In contrast, decreasing the temperature makes the coercivity increase due to the reduction of thermal fluctuation. In addition, as discussed above, the natural angle (easy magnetization direction) remains almost unchanged in the temperature region $0.2 < T < T_c$. Therefore, the three factors together determine the appearance of a minimum of the coercivity in Figure 13b. For the cluster with the interplay of the uniaxial and configurational anisotropies, the minimum of the coercivity appears when the configurational anisotropy is predominant. While it vanishes when the uniaxial anisotropy is stronger than the configurational anisotropy.

4 Conclusion

Based on the Monte Carlo simulation, we have calculated numerically the thermal magnetization, Curie temperature, hysteresis, coercivity, natural angle and energy distribution for a magnetic cluster. It has been found that, the $T^{3/2}$ Bloch law is well satisfied with $B_{sur} = 3B_{bulk}$ at low temperature ($T < 0.5T_C$) for the PFM cluster and B increases drastically with the reduction of atomic number N, which is consistent with the experimental facts. The size dependence of the Curie temperature has also been found to fit the finite-size scaling theory. The simulated thermal dependence of the coercivity reveals that the coercivity decreases dramatically with increasing temperature in the low temperature region ($T < 0.40$), remains unchanged in the medium temperature region, and decreases again with increasing temperature in the high temperature region. The hysteresis and the spin configurations in different magnetization fields indicate the existence of an easy magnetization direction and an anisotropy resulting from the spin configurations, which is proved further by the simulated natural angle and energy distribution in the clusters. The dip in the $H_c - T$ curves for the PFM and FM clusters with $K < 0.6$ has been well explained. A proposition for the relationship between the natural angle to coercivity has been addressed.

This work was supported by Grants No. G1999064508 for National Key Project for Basic Research of China, and Foundation for University Key Teacher by the Ministry of Education, and NSF of Fujian Province (E0320002).

References

1. Jing Shi, S. Gider, K. Babcock, D.D. Awschalom, Science **271**, 737 (1996)
2. D.M. Coex, D.J. Trevor, R.L. Whetten, E.A. Rohlfing, A. Kaldor, Phys. Rev. B **32**, 7290 (1985)

3. W.A. de Heer, P. Milani, A. Chatelain, Phys. Rev. Lett. **65**, 488 (1990)
4. I.M.L. Billas, A. Chatelain, W.A. de Heer, Science **265**, 1682 (1994)
5. C.L. Chien, Annu. Rev. Mat. Sci. **25**, 129 (1995)
6. J.S. Moodera, L.R. Kinder, T.M. Wong, Meservey, Phys. Rev. Lett. **74**, 3273 (1995)
7. P. Chen, D.Y. Xing, Y.W. Du, J.M. Zhu, D. Feng, Phys. Rev. Lett. **87**, 107202-1 (2001)
8. J.J. Versluijs, M.A. Bari, J.M.D. Coey, Phys. Rev. Lett. **87**, 026601 (2001)
9. M. Holdenried, B. Hackenbroich, H. Micklitz, J. Magn. Magn. Mater. **231**, L13 (2001)
10. Ning Zhang, Weiping Ding, Wei Zhong, Dingyu Xing, Youwei Du, Phys. Rev. B **56**, 8138 (1997)
11. Zhigao Huang, Zhigao Chen, Kun Peng, Dunhui Wang, Weiyi Zhang, Fengming Zhang, Youwei Du, to be published in Phys. Rev. B **69** (2004)
12. M. Ziese, Phys. Rev. B **60**, R738 (1999)
13. K. Udea, H. Tabata, T. Kawai, Appl. Phys. Lett. **79**, 988 (2001)
14. K. Sato, H. Katayama-Yoshida, Jpn J. Appl. Phys. **39**, L555 (2000)
15. T. Dietl, H. Ohno, F. Matsukura, J. Cibert, D. Ferrand, Science **287**, 1019 (2000)
16. J.M.D. Coey, Phys. Rev. Lett. **27**, 1140 (1971)
17. R.H. Kodama, A.E. Berkowitz, Phys. Rev. Lett. **77**, 394 (1996); R.H. Kodama, A.E. Berkowitz, J. Appl. Phys. **81**, 5552 (1997); R.H. Kodama, A.E. Berkowitz, Phys. Rev. B **59**, 6321 (1999)
18. B. Martinez, X. Obradors, LI. Balcells, A. Rouanet, C. Monty, Phys. Rev. Lett. **80**, 181 (1998)
19. Q.A. Pankhurst, R.J. Pollard, Phys. Rev. Lett. **67**, 248 (1991)
20. F.T. Parker, M.W. Forter, D.T. margulies, A.E. Berkowitz, Phys. Rev. B **47**, 7885 (1993)
21. S. Linderroth, P.V. Hendriksen, F. Bodker, S. Wells, K. Davis, S.W. Charles, S. Morup, J. Appl. Phys. **75**, 6583 (1994)
22. U. Gradmann, J. Magn. Magn. Mater. **100**, 481 (1991)
23. D.J. Zhang, K.J. Klabunde, C.M. Sorensen, G.C. Hadjipanayis, Phys. Rev. B **58**, 14167 (1998)
24. D.T. Pierce, R.J. Celotta, J. Unguris, H.C. Siegmann, Phys. Rev. B **26**, 2566 (1982)
25. P.V. Hendriksen, S. Linderoth, P.A. Lindgard, Phys. Rev. B **48**, 7259 (1993)
26. G.T. Rado, Phys. Rev. B **40**, 407 (1989)
27. J.P. Chen, C.M. Sorensen, K.J. Klabunde, G.C. Hadjipanayis, E. Devlin, A. Kostikas, Phys. Rev. B **54**, 9288 (1996)
28. R.P. Cowburn, J. Phys. D: Appl. Phys. **33**, R1 (2000)
29. R.P. Cowburn, D.K. Koltssov, A.O. Adeyeye, M.E. Welland, Europhys. Lett. **48**, 221 (1999)
30. R.P. Cowburn, A.O. Adeyeye, M.E. Welland, Phys. Rev. Lett. **81**, 5414 (1998)
31. L. Torres, E. Martinez, L. Lopez-Diaz, J. Iniguez, J. Appl. Phys. **89**, 7585 (2001)
32. R.L. stamp, J. Phys. D: Appl. Phys. **33**, R247 (2000)
33. J.V. Kim, R.L. Stamps, B.V. McGrath, R.E. Camley, Phys. Rev. B **61**, 8888 (2000)
34. E.C. Stoner, E.P. Wohlfarth, IEEE Trans. Magn. **27**, 3475 (1991)
35. Zhigao Huang, Youwei Du, Phys. Lett. A **300**, 641 (2002)
36. K. Binder, D.W. Heermann, *Monte Carlo Simulation in Statistical Physics* (Springer, Berlin, 1992)
37. I. Horio, X.Z. Zhou, A.H. Morrish, J. Magn. Magn. Mater. **118**, L279 (1993)
38. J. Merikoski, J. Timonen, M. Manninen, Phys. Rev. Lett. **66**, 938 (1991)
39. D.L. Mills, A.A. Maradudin, J. Phys. Chem. Solids **28**, 1855 (1967)
40. D.L. Mills, Solid State Phys. **4**, 28 (1971)
41. D.L. Mills, Solid State Phys. **4**, 95 (1972)
42. S.N. Kaul, T.V.S.M. Mohan Babu, J. Phys.: Condens. Matter **1**, 8509 (1989)
43. T. Kaneyoshi, *Amorphors Magnetism* (CRC Press, Boca Raton, 1984)
44. Heng Lai, Zhigao Huang, Intermetallics **8**, 655 (2000)
45. H. Kachkachi, A. Ezzir, M. Nogues, E. Tronc, Eur. Phys. J. B **14**, 681 (2000)
46. M.N. Barber, in *Phase Transitions and Critical Phenomena*, edited by C. Domb, J.L. Lebowitz (Academic, New York, 1983), Vol. 8, p. 145
47. D.P. Landau, Phys. Rev. B **14**, 255 (1976)
48. D.A. Dimitrov, G.M. Wysin, Phys. Rev. B **51**, 11947 (1995)
49. O. Iglesias, A. Labarta, Phys. Rev. B **63**, 184416-1 (2001)
50. C.P. Bean, Livingston, J. Appl. Phys. **30**, 120S (1959)
51. H. Pfeiffer, W. Schuppel, Phys. Status Solidi (a) **119**, 259 (1990)
52. S.U. Jen, C.Y. Lee, Y.D. Yao, J. Magn. Magn. Mater. **96**, 82 (1991)
53. C. Johansson, T. Aklint, M. Hanson, M. Andersson, N. Tarras-Wahlberg, E. Olsson, B. Kalska, R. Wappling, A. Rosen, Nanostructureed Materials **12**, 287 (1999)
54. B. Martinez, A. Roig, X. Obradors, E. Molins, J. Appl. Phys. **79**, 2580 (1996)
55. B.N. Bhowmik, R. Ranganathan, J. Magn. Magn. Mater. **248**, 101 (2002)
56. Zhigao Huang, Zhigao Chen, Fengming Zhang, Youwei Du, unpublished